Flow, Turbulence and Combustion (2026) 116:50
https://doi.org/10.1007/s10494-026-00748-w

RESEARCH

Comparison between Localized Skin-Friction Reduction and Suction on a Supercritical Airfoil

Annika Frede[1] · Giulio Soldati[2] · Sergio Pirozzoli[2] · Niccolò Berizzi[3] · Maurizio Quadrio[3] · Davide Gatti[1]

Received: 8 February 2026 / Revised: 6 April 2026 / Accepted: 7 April 2026

Abstract
In this work, direct numerical simulations are used to investigate which physical effects of active flow control are most relevant for improving the aerodynamic performance of airfoils. To this end, two active flow control strategies based on inherently different physical mechanisms are systematically compared on the upper surface of the supercritical V2C airfoil in compressible transonic flow. The first strategy consists of streamwise-travelling waves of spanwise wall velocity (StTW), a skin-friction drag reduction technique that locally decreases wall shear stress in the region of application. The second strategy is uniform wall-normal suction, which locally increases skin-friction drag. One strength of the present study is that the control configurations are evaluated at matched lift coefficients to isolate the impact of the control mechanisms on drag components, boundary-layer development, shock position, and energetic cost. Despite their opposite local effects on skin-friction drag, both control strategies yield comparable and significant improvements in global aerodynamic efficiency. The analysis reveals that, for both approaches, the dominant mechanism responsible for the efficiency increase is a downstream displacement of the shock, accompanied by a reduction in boundary-layer momentum thickness. These results highlight the central role of shock–boundary-layer interaction control in enhancing transonic aerodynamic performance and demonstrate that skin-friction drag reduction alone is not a sufficient metric for assessing the effectiveness of active flow control strategies.

Keywords Flow control · Turbulent boundary layer · Transonic flow · Travelling waves · Suction

✉ Annika Frede
annika.frede@kit.edu

[1] Institute of Fluid Mechanics, Karlsruhe Institute of Technology, Kaiserstr. 10, 76131 Karlsruhe, Baden-Württemberg, Germany

[2] Dipartimento di Ingegneria Meccanica e Aerospaziale, Sapienza Università di Roma, Via Eudossiana 18, 00184 Roma, Italy

[3] Dipartimento di Scienze e Tecnologie Aerospaziali, Politecnico di Milano, Via La Masa 34, 20156 Milano, Italy

Published online: 11 May 2026

1 Introduction

Anthropogenic climate change, driven by rising CO_2 emissions among other causes, represents one of the most significant challenges in the 21^{st} century as far as engineering sciences are concerned. Aviation accounts for about 2.4% of the global annual CO_2 emissions and contributes 4% to human-induced global warming with increasing trends (Klöwer et al. 2021). To address these challenges, the aviation industry needs to improve aircraft efficiency. One promising approach is the use of flow control techniques that modify boundary layer behavior in various ways to enhance aerodynamic performance. Among the possible objectives, drag reduction is particularly important as it contributes directly to lowering CO_2 emissions and enhancing overall aircraft performance.

Over the last decades, numerous drag reduction techniques have been proposed and investigated (Gad-el Hak 2000; Spalart and McLean 2011), many of which specifically target turbulent skin-friction drag. These strategies are typically categorized into active and passive control methods. Passive methods operate without external energy input and typically involve geometric modifications of the surface. Such modifications can help to delay transition toward the trailing edge or reduce the risk of flow separation, thereby lowering the skin-friction drag. Among the most successful passive approaches are riblets, a type of surface structuring that has been shown in laboratory experiments to reduce skin-friction drag by about 10% (Bechert et al. 1997). Flight tests on transport aircraft later confirmed these results, demonstrating friction drag reductions of 2–6% (Walsh et al. 1989; Szodruch 1991). Although passive methods generally offer moderate drag reduction and tend to be effective only near specific operating conditions, their simplicity, low energetic cost, and minimal impact on weight and maintenance make them attractive for practical applications.

Active control methods, in contrast, require an external energy input but can be tuned to a broader range of flow conditions and have the potential to achieve larger drag reductions. However, their overall benefit must be evaluated by considering both the achieved drag reduction and the energy costs associated with the actuation.

Spanwise forcing is a class of active flow control strategies that has attracted significant interest among researchers over the last few decades because of its relative simplicity and effectiveness (Ricco et al. 2021). The simplest implementation is the spanwise oscillating wall, in which the wall undergoes spatially uniform but time-varying motion (Jung et al. 1992; Quadrio and Ricco 2004). A more effective variant combines both temporal and spatial modulation and is referred to as streamwise-travelling waves of spanwise velocity (StTW) (Quadrio et al. 2009). In this approach, the following velocity distribution is imposed at the wall

$$w_w(x,t) = A\sin(\kappa_x x - \omega t), \tag{1}$$

with the amplitude A, the spatial and temporal frequencies of the wave κ_x and ω, respectively, and the streamwise and temporal coordinates, x and t. StTW have been extensively studied in both experiments and numerical simulations. For example, Auteri et al. (2010) reported friction drag reduction of up to 33% in turbulent pipe flow using a segmented rotating wall setup, confirming earlier direct numerical simulation (DNS) findings. More recent investigations in planar actuated systems also demonstrated substantial drag reduction per-

formance (Marusic et al. 2021; Knoop et al. 2024). Overall, StTW have consistently been shown to reduce friction drag in turbulent channel flows and other canonical configurations.

Another example of an active control method is wall-normal homogeneous blowing and suction. In this technique, a small amount of mass is injected into the flow (blowing) or removed from it (suction) through the wall to manipulate boundary layer development. Suction was already investigated by Prandtl and Betz (1932), who demonstrated that it can prevent boundary layer separation in regions with an adverse pressure gradient. Subsequent studies on porous flat plates showed that suction delays the laminar-turbulent transition, whereas blowing tends to promote it (Mickley et al. 1954; Black et al. 1958), consistent with Prandtl's early observations. Blowing was also found to increase boundary layer thickness and reduce skin-friction drag, while suction had the opposite effect. These experimental observations were later confirmed by direct numerical simulations (Sumitani and Kasagi 1995; Park and Choi 1999). Further analysis by Hwang (2004) demonstrated that blowing can reduce friction by about 50% in subsonic and up to 80% in transonic flat plate configurations. Overall, blowing effectively reduces friction drag in planar or flat plate geometries, whereas suction increases it.

The active control methods of StTW and blowing have demonstrated positive results in reducing friction drag in channel and flat plate geometries. However, most studies of such flow control techniques have been limited to these simplified configurations, in which skin-friction drag is the only source of drag. In addition, some investigations do not account for the energetic cost of active control, and therefore do not report the resulting net drag savings, which combine the reduction in friction drag and the power required for actuation. In realistic aerodynamic applications, such as airfoils, complex geometry, surface curvature, pressure drag, and control energy requirements all play significant roles, making the connection between local friction drag reduction and overall aerodynamic efficiency considerably more complex.

Most studies of StTW have been conducted in incompressible, planar flows at low Reynolds numbers, while investigations of compressible flows and non-planar geometries remain poorly explored. Some progress toward addressing this gap has been made in recent years. A DNS study conducted by Banchetti et al. (2020) of a channel with a bump on the lower wall demonstrated that StTW affect the pressure drag but remain effective in reducing the overall drag. Furthermore, Gattere et al. (2024) showed that StTW remain effective even in compressible and supersonic regimes in a channel flow. The first investigation combining both a curved surface and compressible flow was conducted by Quadrio et al. (2022), who applied StTW to a fraction of the upper side of a transonic airfoil. The study reported a local reduction in friction drag and an improvement in aerodynamic efficiency, primarily due to an increase in lift caused by a control-induced downstream shift of the shock, accompanied by a rise in its intensity. An extension of this work by Berizzi et al. (2025), based on a parametric study, observed a similar shock displacement toward the trailing edge and reported friction-drag reductions and efficiency gains of approximately 11%. A sketch of StTW on an airfoil is shown in Fig. 1b). Collectively, these studies extend previous work on simpler geometries and demonstrate that StTW retain their ability to reduce friction drag and enhance aerodynamic efficiency under more realistic aerodynamic conditions.

Motivated by the promising results in simple flow scenarios and by the conceptual simplicity of the actuation, homogeneous blowing and suction have also been investigated in more complex flow configurations. LES simulations of incompressible flow around a

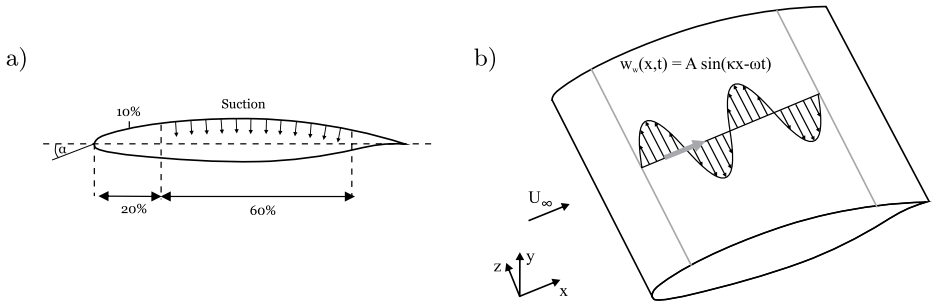

Fig. 1 Sketch of the control mechanisms via (**a**) Suction on the upper side of an airfoil and (**b**) Streamwise-travelling waves of spanwise velocity

NACA4412 airfoil performed by Atzori et al. (2020) showed that uniform blowing on the upper side produced the expected reduction in friction drag. However, it also increased pressure drag and reduced lift, resulting in an overall loss of efficiency. Suction on the upper side exhibited opposite trends, although it increased friction drag, it sufficiently reduced pressure drag and increased lift to yield an efficiency gain at the low Reynolds number considered. A broad RANS-based parametric study by Fahland et al. (2021) confirmed these effects of homogeneous blowing and suction on the drag components. Furthermore, it was found that net drag savings are not guaranteed once the energetic cost of mass injection or extraction is included. The influence of compressibility was examined by Frede and Gatti (2025), who conducted a parametric study of transonic flow around the RAE2822 airfoil. While the general trends in friction and pressure drag were consistent with earlier studies, suction on the upper side in the transonic regime was found to significantly alter the shock position, shifting it downstream and intensifying it, whereas blowing produced opposite effects. Suction locally increased friction drag in the region where it was applied, while blowing reduced it. When friction and pressure drag, as well as actuation costs, were taken into account, low-magnitude suction in high-lift configurations was shown to improve overall efficiency. A sketch of suction control on the upper side is shown in Fig. 1a). Contrary to previous investigations, this study demonstrated that suction can yield a positive efficiency improvement even though it increases the local friction drag.

When applied in the transonic regime, StTW and uniform suction exhibit similar global aerodynamic effects: both yield a sizable increase in lift coefficient, achieved by a downstream shift of the shock, at a comparatively constant total drag coefficient. This is achieved in both cases in spite of the fact that the effect of the two strategies on local skin-friction is opposite: uniform suction increases it while StTW reduces it compared to the reference case. These observations suggest that friction drag reduction may not be the primary driver of the enhanced efficiency, instead, factors such as the downstream shift of the shock and the upstream boundary layer thinning may be more influential. This idea was already discussed by Berizzi et al. (2025).

To better understand the mechanisms responsible for net drag reduction and efficiency enhancement, a systematic comparison of the two control strategies under identical conditions is required. In the present work, the flow control techniques of uniform suction (US) and streamwise travelling waves of spanwise velocity applied to the upper side of the supercritical airfoil V2C in a compressible and transonic flow are investigated. For the compari-

son of the two control techniques, the controlled simulations are performed at the same lift coefficient, to directly see the effect of the applied control on the drag components as well as boundary layer parameters. The study addresses the central question: What are the main factors leading to an efficiency increase in compressible and transonic conditions when applying either suction or StTW, and to what extent do these factors differ between the two approaches? To answer this question, direct numerical simulations are conducted for several control cases as well as a reference simulation of the uncontrolled flow.

The paper is structured as follows: Sect. 2 introduces the numerical approach and computational setup; Sect. 3 presents the results, including the aerodynamic performance and boundary layer evolution; Sect. 4 discussed the additional power input for the active flow control techniques; and Sect. 5 concludes the manuscript with a discussion of the findings.

2 Methodology

2.1 Numerical Methods

Direct Numerical Simulations of the turbulent flow are performed with the solver FLEW, developed by Soldati et al. (2024), which is based on the work of Pirozzoli (2011b). FLEW is specialized for simulations of compressible flow over complex geometries, such as airfoils, and extends the Cartesian-based solver STREAmS (Bernardini et al. 2021) to curvilinear structured grids while preserving the high efficiency and state-of-the-art numerical schemes.

The computational domain is discretized using a structured hexahedral grid, which enables the use of standard finite-difference techniques. The compressible Navier-Stokes equations are solved with a hybrid numerical scheme proposed by Pirozzoli (2011a). This approach combines central schemes, which minimize the numerical dissipation and are ideal for accurately resolving turbulent structures, with Weighted Essentially Non-Oscillatory (WENO) schemes (Liu et al. 1994), which are essential for capturing shock waves. Since central schemes can be prone to nonlinear instabilities, FLEW employs a stabilization technique based on the skew-symmetric splitting of convective derivatives (Pirozzoli 2011a), which preserves the global kinetic energy in the inviscid and low Mach number regime.

The spatial derivatives are first calculated in the computational space and then transformed into the physical space using metric coefficients, which are derived from the geometry of the physical mesh. The same schemes used for the convective derivatives are employed to compute the metric terms to preserve a uniform free stream (Visbal and Gaitonde 2002), which is essential for complex geometries. Central differencing achieves eighth-order accuracy for both convective and viscous terms, while the WENO discretizations reach seventh-order accuracy.

FLEW is optimized for large-scale simulations on high-performance computing systems. It supports scalable parallelism via the Message Passing Interface (MPI) and is fully compatible with modern GPU-based architectures widely used in supercomputing facilities.

2.2 Computational Setup

The body-fixed coordinate system is defined with its origin located at the airfoil leading edge. The x-axis is aligned with the chord line and directed downstream, the y-axis is normal to the chord and oriented upward, and the z-axis is oriented spanwise. A second reference frame, the local surface coordinate system, is introduced for the analysis of the boundary layer characteristics. In this system, the tangential coordinate ξ lies along the local surface tangent, while the normal coordinate η corresponds to the direction of the local surface normal. The two coordinate systems are sketched in Fig. 2a).

The present study investigates the supercritical airfoil V2C, originally designed within the European project TFAST (Doerffer et al. 2021). Additional information, such as polar plots and angle of attack dependencies, is shown in the Appendix A. The simulations are performed at an angle of attack of $\alpha = 4°$, which corresponds to the point of the maximum lift-to-drag ratio. The chord based Reynolds number is set to $Re_\infty = U_\infty c/\nu_\infty = 3 \times 10^5$, where U_∞ is the free stream velocity, ν_∞ the kinematic viscosity, and c the chord length. The free-stream Mach number is $Ma_\infty = U_\infty/a_\infty = 0.7$, with a_∞ denoting the speed of sound at free stream conditions.

To enforce a steady laminar-to-turbulent flow transition on both sides of the airfoil $0.1c$ downstream from the leading edge, a numerical tripping in the form of a localized small Gaussian blob of wall-normal random volume forcing is applied (Schlatter and Örlü 2012). The tripping force is set to $150U_\infty^2/c$, ensuring the proper development of a fully turbulent boundary layer. The displacement thickness is approximated with $\delta = 0.001c$ at the tripping location to calculate the length scales of the tripping parameters as the spanwise wavelength $\lambda_z = 1.7\delta$, and the spatial Gaussian attenuation of the forcing region $L_x = 4\delta$ and $L_y = \delta$, as well as the period $T = L_x/U_\infty$.

The characteristic length c and the free-stream velocity U_∞ are used as reference scales to non-dimensionalize all quantities and the governing equations. In addition to these outer scales, a viscous scaling is introduced, where the friction velocity $u_\tau = \sqrt{\tau_w/\rho}$ serves as the velocity reference and the viscous length scale ν/u_τ as the reference length. Here, τ_w, ρ, and ν denote the wall shear stress, fluid density, and kinematic viscosity, respectively. Variables normalized using viscous units based on the reference case (i.e., without active flow control) are denoted with a superscript '+', while those scaled by the friction velocity of each case carry a superscript '*'. It is important to note that the wall shear stress exhibits

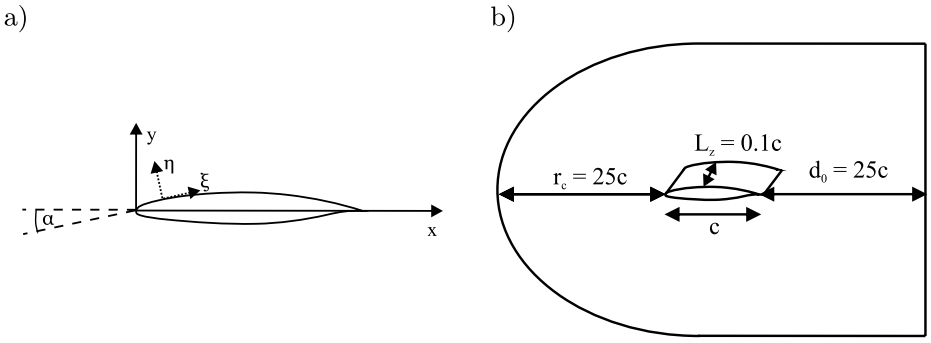

Fig. 2 (**a**) Sketch of the different coordinate systems used for the analysis of the simulation, and (**b**) Sketch of the mesh and the corresponding length scales

significant spatial variations along the surface. In this study, friction-related quantities are evaluated on the upper side at $x = 0.35$. This location is chosen because it lies sufficiently downstream for the effects of actuation to develop, yet remains far enough upstream of the shock region for the wall pressure gradient to remain approximately constant across all cases. Berizzi et al. (2025) also chose a fixed position to evaluate the friction-related quantities and showed that the choice does not impact the qualitative form of the results.

The computational mesh has a C-type topology and consists of $4096 \times 512 \times 256$ cells. In radial direction, the domain extends up to 25 chord lengths, while the spanwise extent is $L_z = 0.1$. The spanwise depth of the computation domain is sufficient to accommodate all relevant turbulent structures and for achieving spanwise decorrelation of the flow (Quadrio et al. 2022; Berizzi et al. 2025). Grid cells are uniformly spaced in the spanwise direction, while a hyperbolic tangent distribution is used in the wall-normal direction. The mesh resolution satisfies the criteria for a fully resolved DNS, with near-wall spacings of $\Delta x^+ < 10$ (streamwise), $\Delta y^+ < 0.5$ (wall-normal), and $\Delta z^+ < 5$ (spanwise). A schematic sketch of the computational domain is shown in Fig. 2b).

Periodic boundary conditions are applied in the spanwise direction. At the far field, non-reflecting boundary conditions based on the characteristic wave approach (Poinsot and Lelef 1992) are used to prevent the reflection of pressure waves back toward the airfoil. In the reference case, the airfoil surface is modeled with no-slip, adiabatic wall conditions. For the flow-control cases, the boundary conditions are modified: spanwise wall motion is imposed for the StTW approach, while a prescribed wall-normal velocity is applied for suction control.

Time integration is performed using a third-order Runge-Kutta scheme with a maximum Courant-Friedrichs-Lewy number of $CFL = 1$. Flow quantities are averaged in both time and spanwise direction, over a minimum interval of $\Delta T = 40$, excluding an initial transient period that is determined individually for each case. The statistical convergence of the lift and drag was assessed a posteriori using the procedure proposed by Russo and Luchini (2017). For all configurations, the uncertainty in the estimated mean lift coefficient, measured by the ratio of its standard deviation to the mean value, does not exceed 0.3%, while the corresponding uncertainty for the drag coefficient remains below 0.8%.

2.3 Numerical Database

The control method of StTW is defined by five parameters: the spatial wavenumber κ_x, the temporal frequency ω, the amplitude A, and the streamwise positions defining the start and end of the control region, x_b and x_e. In this study, the control region is fixed between $x_b = 0.2$ and $x_e = 0.78$ for both control methods (Fahland et al. 2021; Quadrio et al. 2022). The upstream limit is chosen sufficiently upstream to allow the flow to transition to fully developed turbulence, while the downstream limit ensures that possible trailing edge components, such as, for example, flaps or ailerons, remain outside the control domain. The wall velocity is defined as in Equation 1.

For both control methods, a smoothing function (Yudhistira and Skote 2011) is applied over a distance of $\Delta x_{smooth} = 0.05$ at the beginning and end of the control region to ensure a smooth transition between the uncontrolled and controlled flow. The smoothing function is given by

$$f_{smooth}(x) = \frac{1}{2}\left[\tanh\left(\frac{x - x_b}{\Delta x_{smooth}}\right) - \tanh\left(\frac{x - x_e}{\Delta x_{smooth}}\right)\right], \tag{2}$$

where, for the StTW control, both the spanwise momentum and the energy are corrected according to the imposed wall velocity.

In the case of suction control, the governing parameter is the wall-normal suction velocity u_{us}, normalized by the free-stream velocity U_∞. The steady wall velocity is computed as

$$u_w(x) = f_{smooth}(x)\, u_{us}, \tag{3}$$

where the suction velocity components are projected using the local grid metrics to ensure the control is applied normal to the wall. The energy correction is the same as applied for the travelling wave control case.

Three representative StTW configurations are investigated: SW1 (streamwise wave), where the control has the shape of a steady wave; SW2, a configuration that showed the a large reduction in the friction coefficient combined with a large increase in efficiency in previous studies (Berizzi et al. 2025); and SW3, a configuration with a reduced wave amplitude compared to the other ones. A baseline reference case (REF) without flow control is also computed. All simulations are conducted at an angle of attack of $\alpha = 4°$.

To compare the two control methods, each suction case was iteratively tuned such that its lift coefficient matched the corresponding StTW controlled case at a constant angle of attack of $\alpha = 4°$. The lift coefficient was selected as the matching parameter to test the hypothesis regarding whether the primary contributor to the improved efficiency is the reduction of the friction drag or the modification of the shock position. A RANS simulation with the open source code SU2 (version 8.1.0) was conducted to estimate the initial suction velocity for the DNS setup. Note that the lift coefficient of the SW1 and SW3 cases is nearly identical, compare Table 1, thus there is only one suction case (US1) for the comparison of these two cases. Consequently, the suction cases were adjusted to match the lift coefficients of the corresponding StTW configurations. The comparison between the control methods is therefore carried out at identical lift coefficients and angles of attack. The complete set of configurations is summarized in Table 2

3 Results

In this section of the manuscript, the effectiveness of the two investigated control methods is discussed. Therefore, the force coefficients as well as the changes in the distribution of the shear stress and pressure along the surface are shown. Further, the boundary layer proper-

Table 1 Summary of the performed simulations with the corresponding control parameters. The travelling waves configurations are characterized by the amplitude A, and the spatial κ_x and temporal ω frequencies of the wave. The suction cases are characterized by the uniform suction velocity u_{us}

Case ID	$\kappa_\mathbf{x}$	ω	$\mathbf{A}$	$\mathbf{u_{us}}$
REF	-	-	-	-
SW1	108.6	0	0.826	-
SW2	108.7	39.8	0.826	-
SW3	108.6	39.8	0.438	-
US1	-	-	-	0.00105
US2	-	-	-	0.0012

Table 2 Aerodynamic coefficients for the simulated DNS cases for the reference case, as well as the cases with the control via StTW and suction. The lift c_L and drag coefficient c_D are shown with their percentage relative standard deviation σ as well as the two components of the drag ($c_{D,f}$ and $c_{D,p}$). The aerodynamic efficiency E and the position of the shock x_s are also shown. In the right part of the table, the relative change of the drag coefficient and the efficiency is shown with respect to the uncontrolled case

Case ID	$\mathbf{c_L}$	$\sigma_{\mathbf{c_L}}$	$\mathbf{c_D}$	$\sigma_{\mathbf{c_D}}$	$\mathbf{c_{D,f}}$	$\mathbf{c_{D,p}}$	$\mathbf{E}$	$\mathbf{x_s}$	$\mathbf{\Delta c_D}$	$\mathbf{\Delta E}$
REF	0.727	0.27	0.0259	0.46	0.0089	0.0170	28.1	0.467	-	-
SW1	0.803	0.26	0.0254	0.51	0.0074	0.0179	31.6	0.504	−2.12	12.76
SW2	0.818	0.25	0.0260	0.77	0.0078	0.0182	31.4	0.518	0.51	11.98
SW3	0.800	0.20	0.0256	0.39	0.0081	0.0175	31.2	0.506	−1.03	11.11
US1	0.808	0.10	0.0260	0.23	0.0091	0.0169	31.1	0.509	0.30	10.71
US2	0.819	0.10	0.0262	0.23	0.0092	0.0170	31.3	0.515	0.98	11.47

ties are presented to identify the underlying mechanism of the effectiveness of the control methods.

3.1 Aerodynamic Coefficients

The total aerodynamic force $\mathbf{F}_{tot}$ can be calculated from the integrated distribution of the wall shear stress τ_w and the pressure p as follows

$$\mathbf{F}_{tot} = \oint_S \left(-p\hat{\mathbf{n}} + \tau_w \hat{\mathbf{t}}\right) \, dS, \tag{4}$$

where $\hat{\mathbf{n}}$ is the surface normal vector and $\hat{\mathbf{t}}$ the tangential unit vector. The wall shear stress is defined as $\tau_w = \mu \, \partial \mathbf{u}/\partial n$ with the velocity vector $\mathbf{u}$ and the dynamic viscosity μ.

The total force can be decomposed into lift force F_L (normal to freestream), drag force F_D (parallel to freestream), and a side force F_S, perpendicular to both. For a two-dimensional airfoil in symmetric flow conditions, the side force is zero and will not be considered further. The lift c_L and drag c_D coefficients can be calculated as follows

$$c_L = \frac{F_L}{\frac{1}{2}\rho_\infty U_\infty^2}, \tag{5}$$

$$c_D = \frac{F_D}{\frac{1}{2}\rho_\infty U_\infty^2}, \tag{6}$$

with ρ_∞ denoting the free-stream density.

The drag force is further divided into two sub-components, the friction drag $c_{D,f}$ and the pressure drag $c_{D,p}$, which can be calculated from the integrated friction and pressure in the direction parallel to the freestream as follows

$$c_{D,p} = -\frac{\oint_S p(\hat{\mathbf{n}} \cdot \hat{\mathbf{e}}_\mathbf{x}) \, dS}{\frac{1}{2}\rho_\infty U_\infty^2}, \tag{7}$$

$$c_{D,f} = \frac{\oint_S \tau_w(\hat{\mathbf{t}} \cdot \hat{\mathbf{e}}_\mathbf{x}) \, dS}{\frac{1}{2}\rho_\infty U_\infty^2}, \tag{8}$$

with $\hat{\mathbf{e}}_\mathbf{x}$ the unity vector in x-direction.

The aerodynamic efficiency, defined as the lift-to-drag ratio $E = F_L/F_D$, characterizes the lift produced per unit drag. The position of the shock x_s is determined from the location of the maximum density gradient. To assess the effect of the control, some metrics are compared to the uncontrolled reference through the percent relative change

$$\Delta\Phi = 100\frac{\Phi - \Phi_0}{\Phi_0}, \tag{9}$$

where the value taken by a generic metric of interest in the controlled case is denoted by Φ and Φ_0 is the corresponding reference value.

All parameters are averaged in both space and time, and the results are summarized in Table 1, where the lift c_L and drag coefficient c_D are shown with their percentage relative standard deviation σ.

For StTW, the control leads to a clear increase in the lift coefficient compared to the uncontrolled reference case for all cases. The drag coefficient increases slightly by 0.51% for the SW2 case and decreases for SW1 by 2.12%. Overall, the aerodynamic efficiency improves significantly in all cases, with gains of about 11% and a maximum of 12.76% in the SW1 case. These trends agree with the findings of Berizzi et al. (2025), who also reported an overall improvement in the aerodynamic efficiency under the control of StTW.

While the drag coefficient remains almost unchanged by the control, the share of the friction and pressure drag is modified by it. A decrease of the friction drag $c_{D,f}$ can be observed for the controlled cases via StTW, compensated by a corresponding increase in the pressure drag $c_{D,p}$. The control leads to a modified mean velocity gradient near the wall. More interestingly, the control leads to a shift of the shock toward the trailing edge, see increased x_s in Table 1 compared to the reference case.

The control via suction, tuned to yield the same lift coefficient as a respective StTW case, shows a surprisingly similar behavior to StTW despite the different working principle. Suction also increases the lift coefficient, while the changes in the drag coefficient are modest compared to the uncontrolled case. Overall, an increase in efficiency can be observed in the two investigated cases compared to the reference case. In contrast to the StTW, the control with suction modifies the flow differently. Suction removes low-momentum fluid from the boundary layer, which predictably increases the local wall shear stress and thus the friction drag, while at the same time, the pressure drag decreases. However, it simultaneously shifts the shock toward the trailing edge compared to the reference case. The effect of the control on the boundary layer quantities will be discussed in detail in Sect. 3.5. The lift increase and shock displacement observed under the control with suction are consistent with the mechanisms identified in the StTW cases. This further supports the hypothesis that the shift of the shock, rather than the reduction of the friction, is the key factor determining performance improvement.

Overall, the results of the averaged aerodynamic quantities indicate that the decisive factor for enhancing the aerodynamic efficiency is not the reduction of the wall-shear stress, but the ability of the control technique to alter the shock position. This hypothesis will be further discussed in the following sections.

In the following, the controlled cases are compared to the reference case as well as with each other. Therefore, the controlled cases with the same lift coefficient are grouped: (REF,

SW1 and SW3, US1) and (REF, SW2, US2). Note that the lift coefficients for SW1 and SW3 are nearly identical, only one suction case for comparison is available. Since SW2 and US2 exhibit the largest efficiency gains, they are discussed in detail in the following.

3.2 Pressure and Friction Coefficient Distribution

The distribution of the pressure and the friction coefficients, denoted as c_p and c_f, respectively, are shown in Fig. 3 for the reference case (REF), the travelling waves case SW2, and the corresponding suction case US2. The coefficients are defined as follows

$$c_f(x) = \frac{\tau_w(x)}{\frac{1}{2}\rho_\infty U_\infty^2}, \tag{10}$$

$$c_p(x) = \frac{p_w(x) - p_\infty}{\frac{1}{2}\rho_\infty U_\infty^2}, \tag{11}$$

where $\tau_w(x)$ and $p_w(x)$ are the projected wall shear stress and pressure, respectively, and p_∞ is the freestream pressure.

The pressure distribution along the airfoil surface is shown in Fig. 3a). The sudden decrease of c_p (suction peak) at the leading edge is followed by a plateau, which spans until the shock region and is characterized by a near-zero-pressure gradient for all three cases. For the controlled cases, the pressure coefficient is slightly lower in the plateau region, which is one reason for the increase in lift, which was discussed in Subsection 3.1. The shock region is indicated by a strong positive slope of the pressure coefficient. It can be clearly seen that the shock position for both controlled cases is shifted toward the trailing edge ($x_s = 0.515$) compared to the uncontrolled reference case ($x_s = 0.467$). The suction magnitude was tuned to match the lift coefficient of the StTW case, which not only led to the same c_L but also to the same magnitude of the shift of the shock toward the trailing edge. The shock characteristics differ slightly between the two controlled cases. The slope for the control via suction is larger and thus the shock sharper, while for the case with StTW control, the shock region spans wider. The data which are presented in the analysis are averaged results, thus also the position of the shock is an averaged value. The shock is not fixed in space over time, but varies in a region of 1%c around the stated positions x_s above.

The friction coefficient c_f along the surface of the airfoil is shown in Fig. 3b). For improved visualization of the distribution, the values on the lower surface are plotted with a negative sign. The transition at $x = 0.1$ is clearly visible by a peak of c_f in all configurations on both sides of the airfoil. Up until the transition, the friction coefficient is similar in all cases, the flow being laminar. In the region where the control is applied ($0.2 < x < 0.78$), the trends are different. While for the control via StTW a decrease in c_f is observed, as already expected from previous investigations, an increase in c_f can be observed for the suction case. The shock region is indicated by a drop in the friction coefficient. The decrease in the friction coefficient can already be observed upstream of the shock position. As the flow approaches the shock, it already experiences a strong adverse pressure gradient, see Fig. 3a). This leads to a deceleration of the flow and thus a decrease in the wall shear stress as well as an increase in the boundary layer thickness (see Sect. 3.5). At the shock position, the minimum of the drop is reached. Downstream of the shock, the flow is subsonic, and the

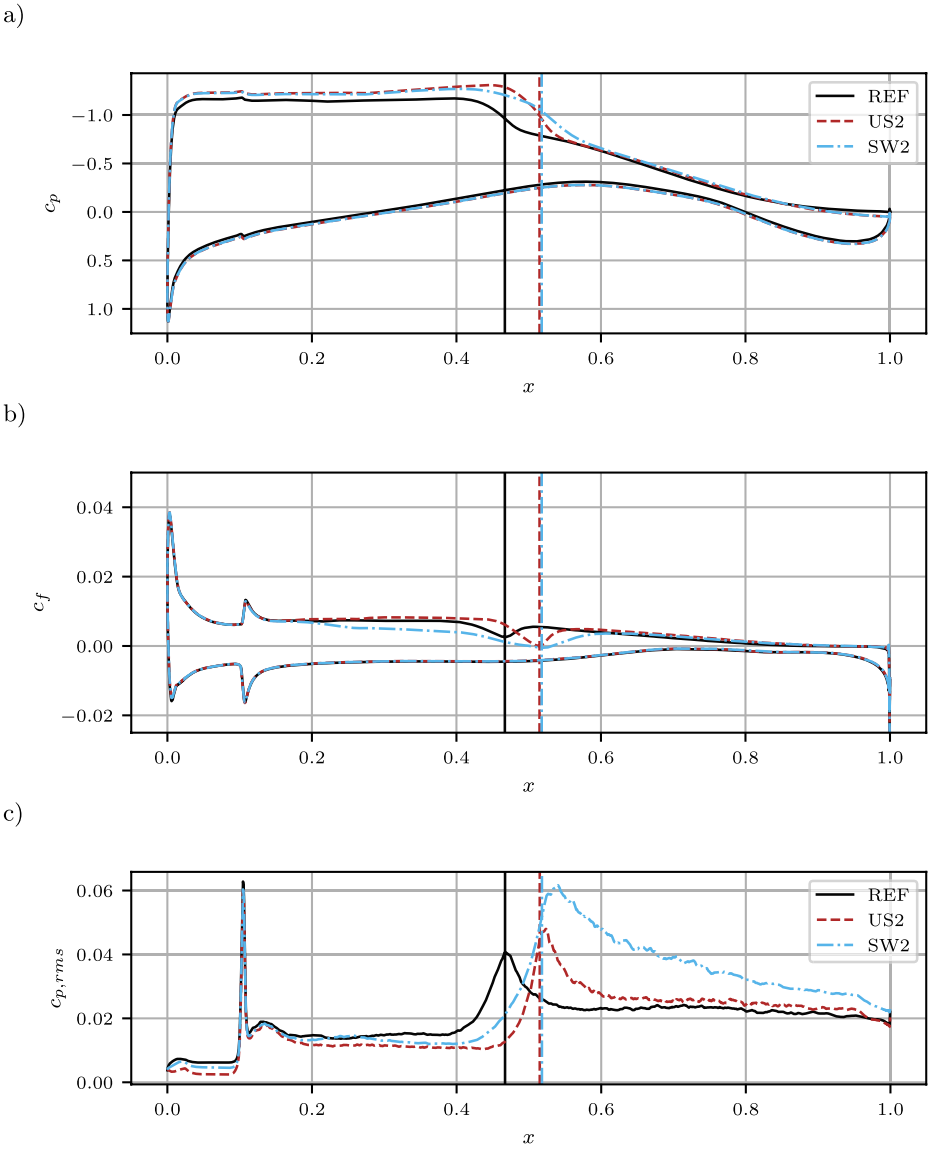

Fig. 3 (**a**) Pressure c_p and (**b**) Friction c_f coefficient distribution along the surface of the airfoil. The vertical lines indicate the shock position

turbulence activities are enhanced due to the shock, leading to increased mixing and thus an increase in wall-shear stress. The drops of c_f in the controlled cases are placed further to the trailing edge, since the position of the shock is shifted toward the trailing edge. The shock positions are indicated by the dashed lines (note that the shock positions of the controlled cases are at the same location and thus overlap). Throughout and immediately downstream of the shock, values of negative c_f, indicating local flow separation and reattachment, are observed for the SW2 case. Considering only the StTW results, one might infer that the

nearly zero or slightly negative c_f values are the primary factor responsible for the observed drag reduction and efficiency improvement. However, in the suction controlled cases, c_f is larger than in the reference case, becoming nearly zero but still positive only in a small region throughout the shock, suggesting the absence of mean flow separation or recirculation bubbles. Therefore, the hypothesis that the total drag reduction and efficiency increase can only be achieved by the formation of a separation bubble characterized by low or negative c_f values is not supported. Instead, the suction cases demonstrate comparable overall drag reduction without the occurrence of a mean separation. Figure 3c) shows the rms values of the pressure coefficient, $c_{p,rms}$. In all configurations, two peaks can be observed. One at the position where the transition takes place and a second one in the region of the shock. The peaks have the same order of magnitude. The peaks indicate the presence of acoustic noise and thus a change in the pressure coefficient.

Figure 4 shows the other investigated controlled cases as well as the reference case. Overall, the results match the already observed results: the two investigated control methods lead to a shift of the shock toward the trailing edge, which is visible in the pressure as well as in the friction coefficient distribution. Furthermore, these results confirm that the shock is sharper for the suction control and wider for the control via StTW. One reason is the difference in the modifications of the boundary layer induced by the two control strategies. While uniform suction reduces both displacement and momentum thickness by a similar amount,

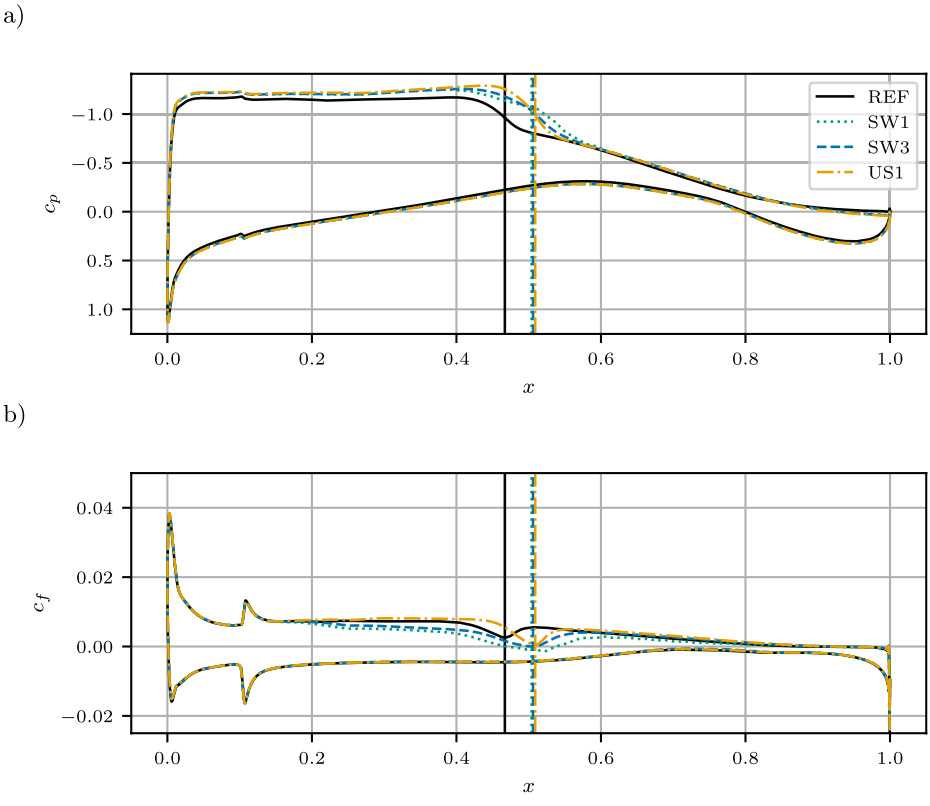

Fig. 4 (**a**) Pressure c_p and (**b**) Friction c_f coefficient distribution along the surface of the airfoil. The vertical lines indicate the shock position

StTW primarily reduce the momentum thickness while maintaining a comparatively larger overall boundary layer thickness. As a result, although the shock position correlates well with the reduction in momentum thickness and is therefore similar for both control methods, the thinner boundary layer in the suction case is less effective at smoothing the strong streamwise pressure gradients associated with the shock. In contrast, the thicker boundary layer in the StTW case leads to a more pronounced smearing of these gradients, resulting in a wider shock structure. Furthermore, in the friction distribution, the separation of the flow for the control via StTW is observed, while the values for suction are close to zero, but do not show a large region of negative values.

One reason for the wider shock in the StTW cases might be the presence of a separation bubble. The presence of a separation bubble makes the shock smoother by an upward shift of the shock penetration into the boundary layer. The separation probability and therefore the presence of a separation bubble are further discussed in Subsection 3.4. Further, in the cases of SW, less turbulence is present compared to the suction cases. In the suction case, the disturbances are pulled toward the wall and thus lead to a sharper shock.

Overall, in all investigated cases (compare Figs. 3 and 4), the same trends can be observed. First, the applied control of suction and StTW shift the shock toward the trailing edge, leading to an increase in the lift coefficient. The suction rate is tuned to achieve the same lift coefficient as the StTW case, the resulting shock position and overall aerodynamic efficiency are nearly identical. Second, this same effect on the shock position and lift coefficient occurs even though the two strategies act differently on the local friction: StTW reduces it, while suction increases it. Third, the effect on the pressure drag is opposite, StTW lead to an increase, while suction decreases the pressure drag. The observations indicate that the turbulent friction drag reduction is only indirectly responsible for the improvement in the aerodynamic efficiency. The dominant contribution instead arises from the shock displacement, which is likely linked to the thinner boundary layer produced by the applied control with respect to the reference case. This aspect will be further examined in Sect. 3.5.

3.3 Pressure and Friction Drag

This section focuses on the distribution of the friction and pressure drag along the airfoil surface. Since the control is applied on the upper side, the effects on the pressure side are negligibly small, and the discussion of the results concentrates on the upper side.

The distribution of $c_{d,f}$ and $c_{d,p}$ for the reference case and the two controlled cases (SW2 and US2) is shown in Fig. 5a and b). The distribution of the friction drag on the upper side closely resembles that of the skin-friction coefficient c_f, see Fig. 5a), as the airfoil surface is nearly flat (except near the leading edge) and therefore mostly parallel to the freestream. The difference in friction drag between the controlled and reference cases $\Delta c_{d,f}$ is shown in Fig. 5c). Four distinct regions can be identified:

- Upstream of control ($x < 0.15$): differences between the cases are small and negligible.
- Pre-shock region ($0.15 < x < 0.4$): the two control strategies yield opposite effects. Suction increases $c_{d,f}$ compared to the reference case, while StTW reduces it.
- Shock region ($0.4 < x < 0.6$): a sharp drop in $c_{d,f}$ marks the shock. Because the shock is displaced downstream in the controlled cases, positive and negative peaks appear in $\Delta c_{d,f}$, reflecting the shifted location of the dip.

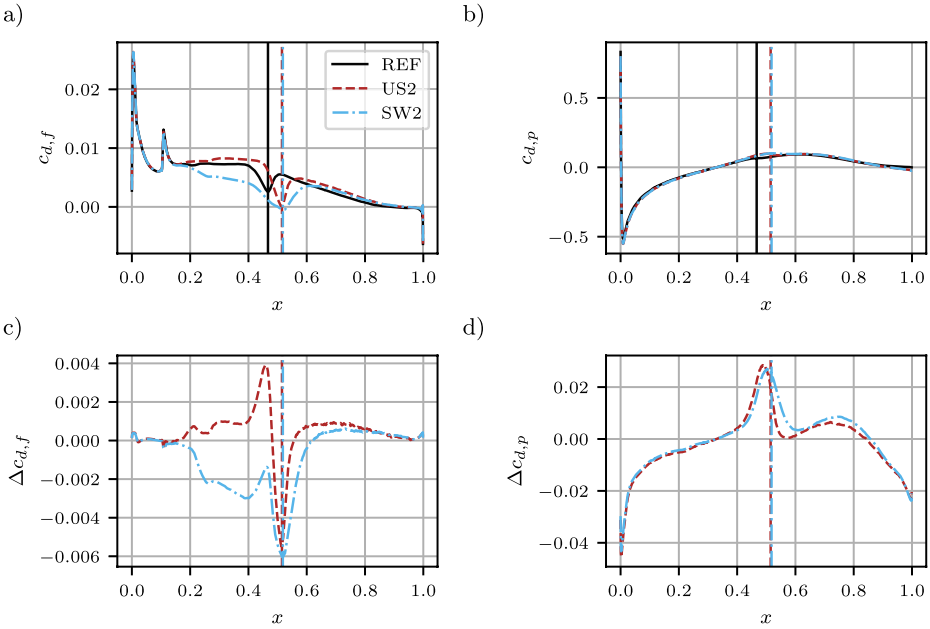

Fig. 5 (**a**) Friction and (**b**) Pressure drag distribution along the spanwise coordinate of the airfoil as well as the differences between the controlled cases and the reference case for the friction and pressure drag (**c**) and (**d**)

- Post-shock region ($x > 0.6$): both control methods exhibit a slight increase in $c_{d,f}$, relative to the reference. At the end of the control ($x = 0.78$), the boundary layer is thinner than in the respective reference case, thus the friction will be locally higher than in the reference case (Stroh et al. 2016).

The changes in the pressure distribution $c_{d,p}$ seem small, but since its absolute magnitude is larger than that of the friction drag, even small variations significantly influence the total drag. The distribution of the pressure drag $c_{d,p}$ is shown in Fig. 5b), which follows a similar trend across all cases: a sharp drop at the leading edge followed by a recovery, and slightly positive values over the control region. Differences emerge near the shock, as seen in Fig. 5d), which presents the distribution of $\Delta c_{d,p}$. Both control methods increase the pressure drag in this region due to the shock being shifted downstream and intensified. The peak of $\Delta c_{d,p}$ is somewhat smaller in height but broader in width for the SW2 case than the US2 case, suggesting that the shock is slightly weaker in SW2. This observation is consistent with the slope changes discussed earlier in Subsection 3.2.

3.4 Instantaneous Velocity Field

The instantaneous velocity profiles of the tangential velocity in the very vicinity of the wall (distance from the wall $1.1 \cdot 10^{-3}c$) are shown in Fig. 6 for the reference case (a), SW2 (b), and US2 (c).

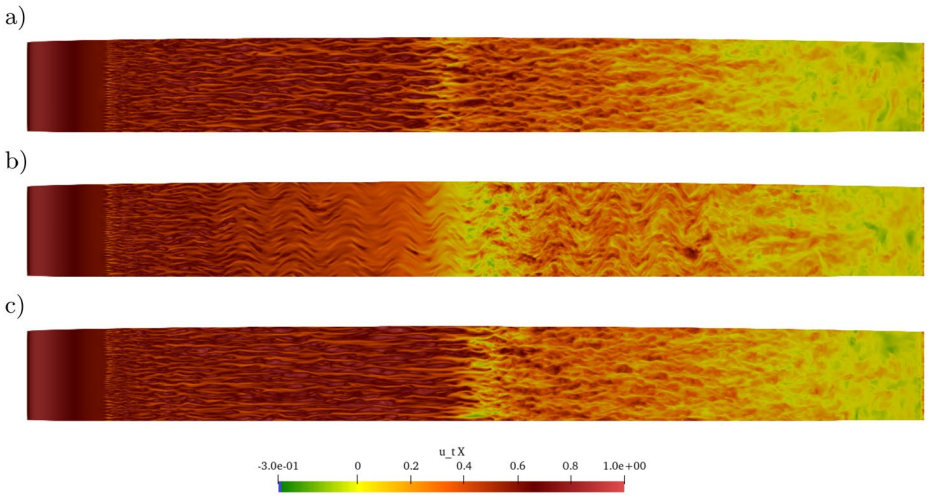

Fig. 6 Instantaneous velocity profiles of the velocity component tangential to the wall on the upper side of the airfoil. The three cases, (**a**) REF, (**b**) SW2, and (**c**) US2, are shown

In all three cases, the flow remains laminar up to the tripping location at $x = 0.1$. In the REF case (see Fig. 6 a), streaks of alternating high and low speed fluid form as the flow transitions to turbulent flow. These streaks are convected downstream and slow down in the vicinity of the shock, where a clear velocity drop is observed. While the time and space averaged skin-friction coefficient c_f remains positive in this case, a few small patches of negative tangential velocity appear in the instantaneous field, indicating the presence of local and instantaneous backflow events. The probability of a negative streamwise velocity ϕ along x is shown in Fig. 7. The probability for a separation in the reference case is close to zero in the region of the shock. Downstream of the shock, the streaks persist but at lower overall velocity levels compared to upstream. Near the trailing edge, a large region of negative velocity develops, indicating flow separation. This agrees with the c_f distribution, which is negative close to the trailing edge. It can also be seen in Fig. 7, where a negative tangential velocity near the trailing edge is present at almost all time steps. The trailing edge separation is due to the geometry of the V2C airfoil, with a fairly steep slope of the upper side near the trailing edge.

The velocity profile for the control via streamwise travelling waves is quite different. The streaks of high and low speed fluid, which are produced as the flow becomes turbulent after transition, can also be observed in this case. In the control region, the effect of StTW is clearly visible in the velocity field, where it induces a wave-like spanwise modulation accompanied by a weakening of the streaks. As the flow approaches the shock, the streaks slow down significantly thanks to the drag-reducing effect of the waves (orange instead of dark red streaks), and the shock itself is shifted downstream compared to the reference case. At the shock position, local regions of negative velocity indicate flow separation, consistent with the negative c_f values discussed previously. The separation probability for the travelling waves cases is between 30% for SW2 and up to 60% for SW1. However, downstream of the shock, the flow reattaches before separating again near the trailing edge, similar to the REF case.

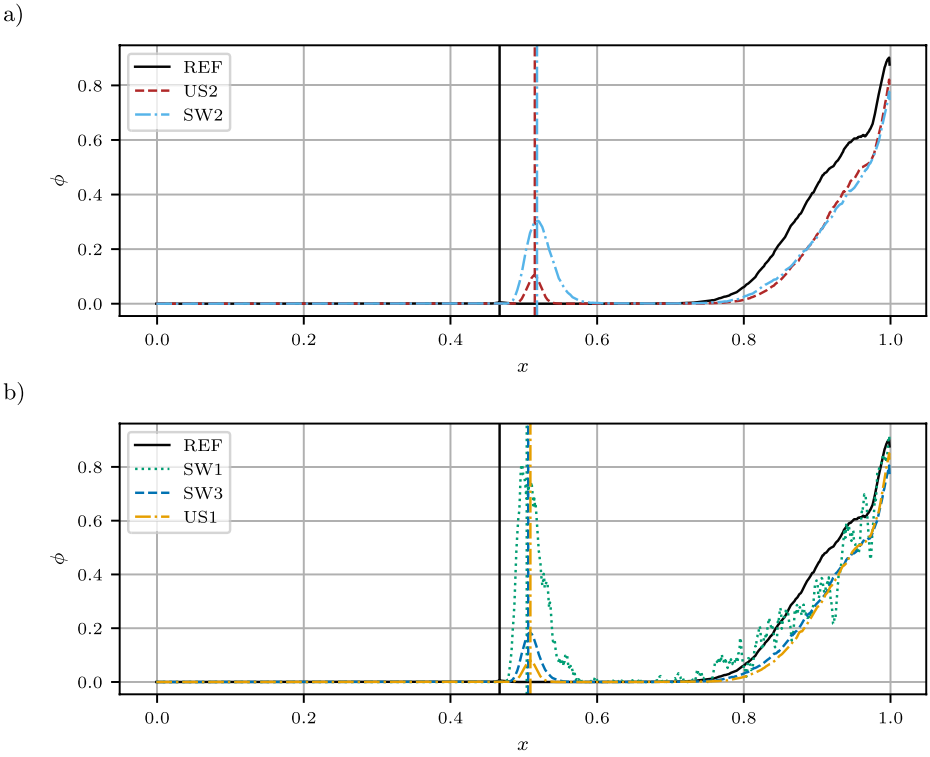

Fig. 7 Separation probability ϕ of the investigated control methods and the reference case. The vertical lines mark the shock positions

The US2 case is similar to the REF case. The shock is shifted downstream, whereby, in this case, there is no slowing down of the flow since suction removes the low-momentum fluid. Although the averaged c_f remains positive, small regions of negative velocity are observed in the shock regions, suggesting the presence of instantaneous backflow events even in the absence of mean separation. The separation probability for the cases with suction control in the region of the shock is approximately 10%. Overall, the control delays flow separation at the trailing edge relative to the reference case. Further, a mean separation is not strictly needed for efficiency gain, as the suction cases reach similar performance without extended separation.

3.5 Boundary Layer Properties

Figure 8 shows the evolution of boundary layer parameters: the displacement thickness δ^*, the momentum thickness θ, and the shape factor H together with the pressure gradient $\partial c_p/\partial x$ along the surface of the airfoil. For a better interpretation of the data the Reynolds number based on the momentum thickness Re_θ is plotted in Fig. 8c).

The boundary layer thicknesses are computed as follows (Xu et al. 2023)

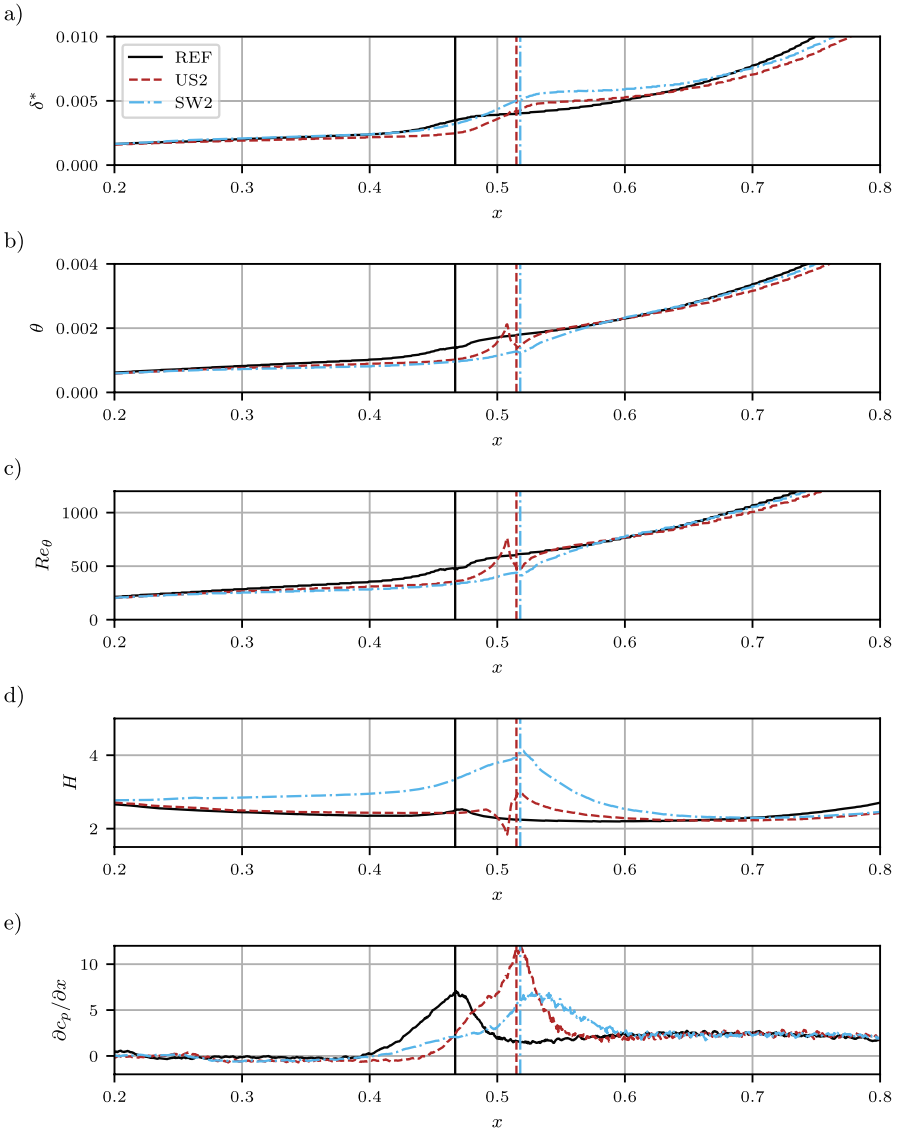

Fig. 8 Integral boundary layer quantities and the pressure gradient along the upper side in the region of the control for the reference case as well as the SW2 and US2 case

$$\delta^* = \int_0^\infty \left(1 - \frac{\bar{\rho}\tilde{u}}{\rho_e U_e}\right) d\eta, \tag{12}$$

$$\theta = \int_0^\infty \left(1 - \frac{\tilde{u}}{U_e}\right) \frac{\bar{\rho}\tilde{u}}{\rho_e U_e} d\eta, \tag{13}$$

$$H = \frac{\delta^*}{\theta}, \tag{14}$$

where $\bar{(\cdot)}$ and $\tilde{(\cdot)}$ denote the Reynolds and Favre averaged quantities, respectively. The edge of the boundary layer is defined as the location where the tangential velocity reaches 99% of the maximum value, denoted by the subscript e. It is noted that in strongly non-equilibrium flows the δ_{99} criterion may become ambiguous Griffin et al. (2021). However, in the present configurations, the separation region is limited, and the δ_{99} criterion remains a consistent measure of the boundary layer thickness.

For all three cases shown in Fig. 8a) the displacement thickness grows gradually. Up to the shock region ($x < 0.4$), the development of the displacement thickness for the REF and the SW2 cases is nearly identical. This can also be observed for the cases SW1 and SW3 in Fig. 9. Thus, the control of suction and StTW do not influence the development of the displacement thickness upstream of the shock. The suction controlled cases exhibit slightly lower displacement thickness compared to both the StTW and reference cases, which can be explained by the removal of the low-momentum fluid.

At the shock location, the external flow changes noticeably. The edge velocity U_e decreases while the pressure and temperature increase abruptly. Since the boundary layer parameters depend on these external quantities, corresponding variations in the thicknesses are observed. Within the shock region, δ^* increases for all cases, with the rise shifted downstream in the controlled configurations owing to the delayed shock position. Immediately downstream of the shock, the displacement thickness is largest for the SW2 case and smallest for the reference case. Both controlled cases show a similar post-shock trend. First, a moderate growth immediately after the shock, followed by a steeper increase toward the end of the control region. The uncontrolled case, by contrast, exhibits a gradual and continuous growth eventually surpassing the controlled configuration so that δ^* becomes largest at the end of the control region.

The airfoil curvature within the control region is limited, and the surface is relatively flat. Therefore, the reduction in the wall-shear stress observed in Fig. 3 for the SW2 case corresponds directly to a weaker growth of the momentum thickness. This behavior is confirmed in Fig. 8b). Both controlled cases show a similar trend. Before the shock, the momentum thickness is lower than in the uncontrolled case. For the control via suction, the momentum thickness is reduced despite higher c_f values, since suction removes low-momentum fluid near the wall, effectively thinning the boundary layer. For the travelling waves case, a smaller θ is consistent with the lower c_f values. Interestingly, the momentum thickness of the corresponding StTW and suction pairs is very similar sufficiently before the shock, even though this has not been imposed explicitly. The fact that this similarity results automatically for those cases featuring similar c_L may suggest that the control-induced modification of the momentum thickness may relate to the increase in c_L and shift of the shock. Across all configurations, the shock induces an increase in the growth rate of the momentum thickness. In the downstream part of the control region, both controlled cases feature slightly smaller momentum thicknesses than the reference case.

The shape factor H remains nearly constant in the reference case but increases significantly in the controlled cases. The increase is moderate for suction control, while the SW2 case exhibits a pronounced peak. A larger H indicates a boundary layer more prone to separation, consistent with the flow separation identified for the SW cases in the c_f distributions, the instantaneous velocity profiles, and the separation probability. The shape factor of a zero-pressure gradient flat plate is in the range of $H \approx 1.6 - 1.7$ (Schlatter and Örlü

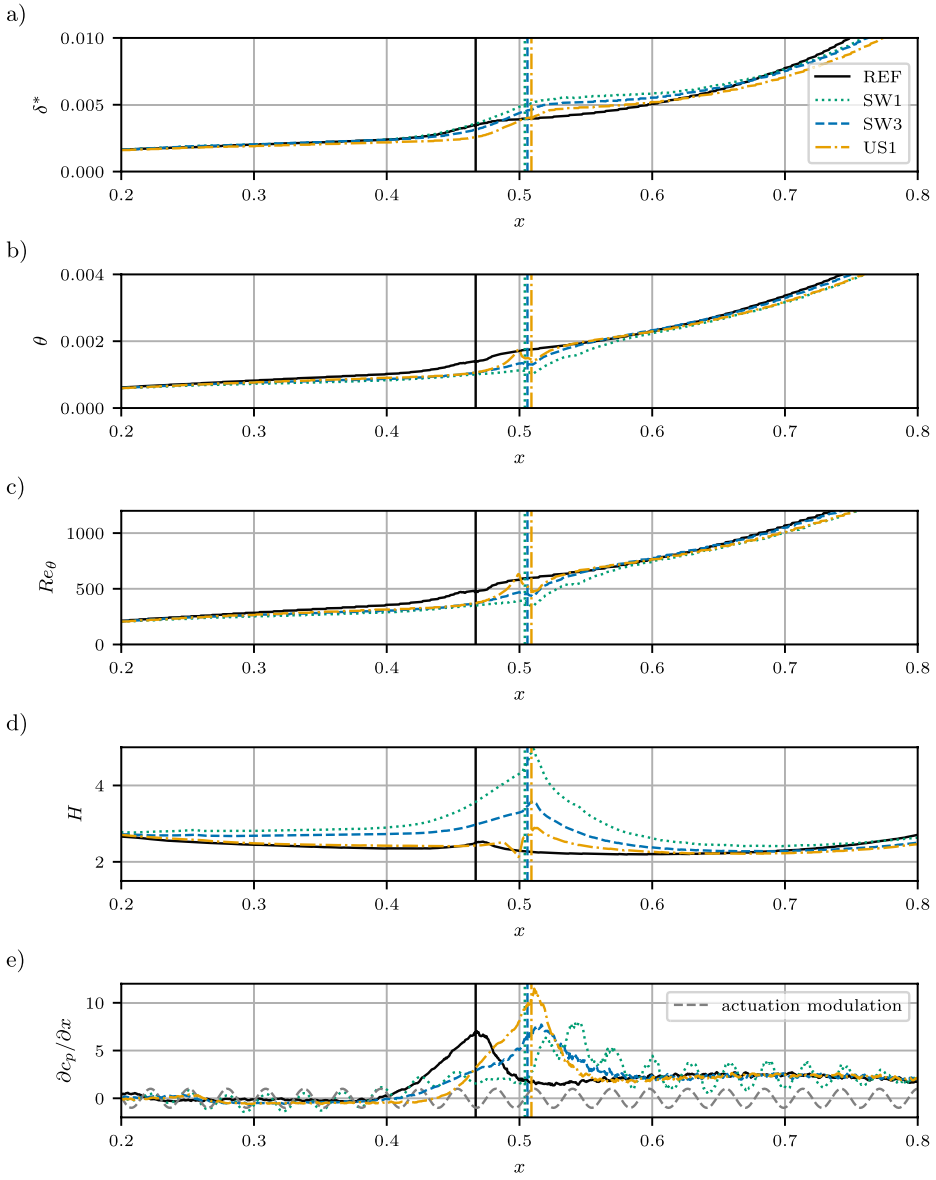

Fig. 9 Integral boundary layer quantities and the pressure gradient along the upper side in the region of the control for the reference case, as well as the SW1 and SW3; and US1 cases. The modulation of the wall for case SW3 is added in d), matching the modulation of the pressure gradient variation

2010) for Reynolds numbers based on the momentum thickness of $Re_\theta \approx 300$. The H factor decreases slightly with increasing Reynolds number for the simplified geometries.

For all cases, an adverse pressure gradient is present in the shock region, (see Fig. 8d), leading to flow deceleration. In the SW2 case, the adverse pressure gradient starts well before the shock, causing earlier flow deceleration. This is consistent with the instantaneous

velocity profiles. The pressure gradient for the SW1 configuration (see Fig. 9d) shows a sinusoidal shape, reflecting the steady modulated wave of the applied control. The control via StTW accelerates and decelerates the near-wall flow at some positions along the steady wave. In the boundary layer, this results in a periodic pressure gradient. Since for the streamwise flow it is equal in which direction the spanwise velocity is directed, the resulting wavelength of the pressure gradient is half the wavelength of the applied steady wave.

The analysis of the boundary layer parameters indicates that, upstream of the shock, the momentum thickness is reduced for both control methods. Furthermore, the momentum thickness exhibits nearly identical values for the two cases. This observation suggests that a reduced momentum thickness upstream of the shock is a contributing factor to the observed improvement in control efficiency.

The analysis of the boundary layer parameters, as well as the distributions of the aerodynamic coefficients, showed that the main contributors to the efficiency increase are the shock displacement toward the trailing edge and the reduced momentum thickness. The Euler solution, representing the inviscid limit with no boundary layer, exhibits the maximum possible shock shift downstream, illustrating the theoretical limit of the achievable control effect. Figure 10 compares the pressure distribution of the present DNS results and the inviscid Euler solution, computed using the open-source solver SU2. It is expected that the positive effect of the control to shift the shock downstream would reduce with increasing Reynolds number, since the boundary layer would become thinner compared to the chord, but the conditions are still far from a vanishing boundary layer thickness, and there is the possibility that these control strategies still yield positive effects at large, albeit not infinite, Reynolds numbers.

Figure 11 presents the wall-normal profiles of the mean streamwise velocity scaled in viscous units, computed at $x = 0.35$. The first two plots ($x = 0.3$ and 0.4) illustrate the upstream region of the shock, where the control already exhibits mild influence while the shock remains downstream. The control does not significantly affect the viscous sublayer before the shock. For StTW, the velocity profile is steeper, indicating a higher tangential velocity component. Downstream of the shock, the profiles flatten due to the flow deceleration, observed in $x = 0.5$ for the reference case and $x = 0.6$ for the controlled case.

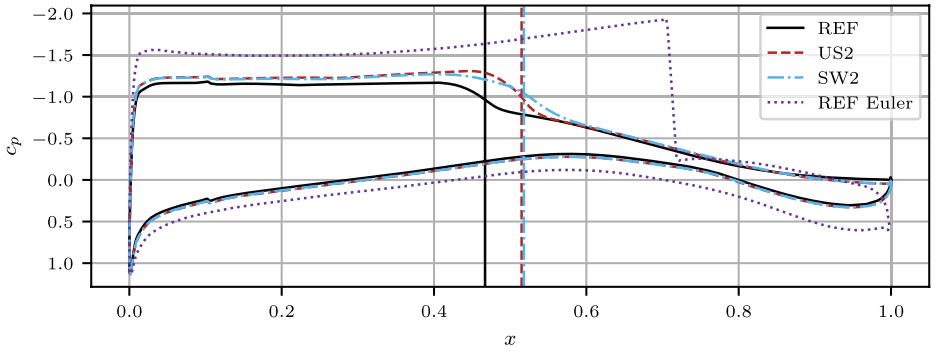

Fig. 10 Pressure distribution of the Euler solution compared to the DNS results

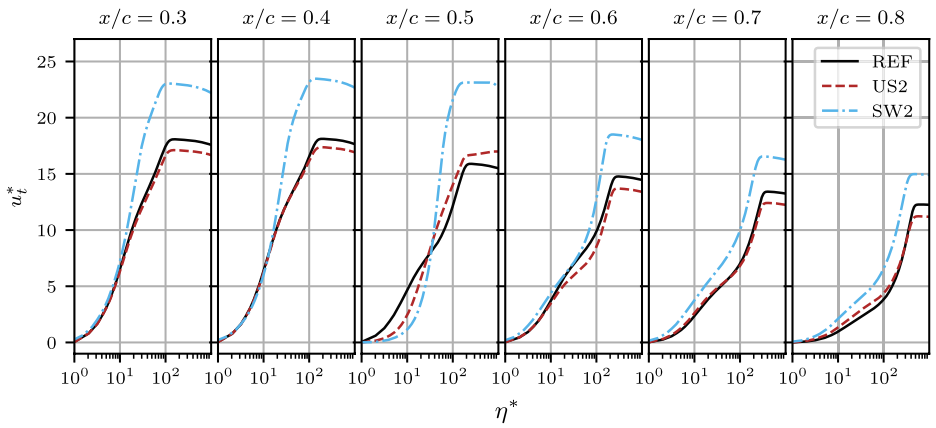

Fig. 11 Wall-normal profiles of the mean streamwise velocity scaled in viscous units at different positions along the upper side of the airfoil. The corresponding viscous units are computed at $x = 0.35$

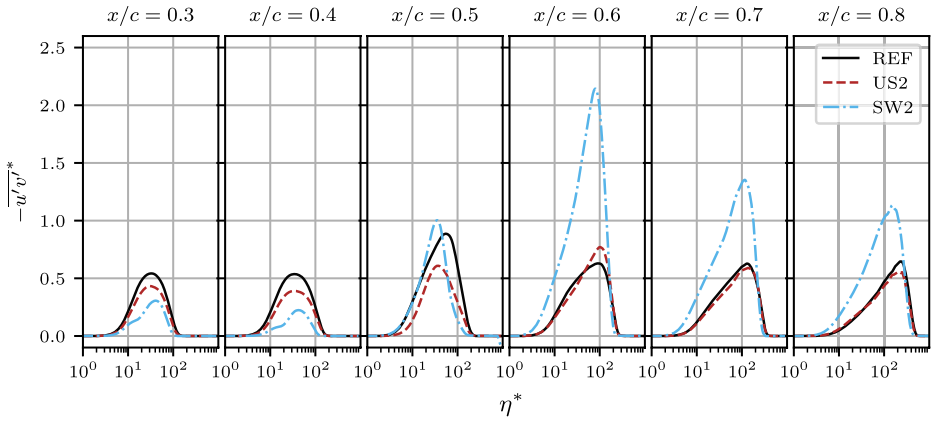

Fig. 12 Tangential turbulent stress scaled in viscous units at different positions along the upper side of the airfoil. The corresponding viscous units are computed at $x = 0.35$

3.6 Reynolds Stresses

The tangential Reynolds stress, scaled in actual viscous units, at six different locations along the upper side is shown in Fig. 12. The stress peaks shift toward higher η^* values when evaluating the tangential Reynolds stresses further downstream. The position of the peak for $x \leq 0.4$ is similar throughout all cases, with a clear reduction in the SW2 case, indicating turbulent suppression. After $x = 0.5$, the effect of the adverse pressure gradient can be observed, which moves the peak outwards. The effect of the shock is more visible in the controlled cases, where higher amplitudes in the $\overline{u'v'}^*$ peaks and a larger shift can be observed. The controlled case SW2 displays the highest peak, this could be due to the presence of the separation bubble, whose shear layers can additionally trigger turbulence.

4 Power Consumption

Active flow control methods require energy to operate. Quantifying the amount of energy employed for operation is essential to assessing the viability of the control. Although both control strategies investigated in the present work, StTW and US, influence the near-wall flow characteristics, they do so through fundamentally different physical processes, which is also reflected in the corresponding power requirements. The following subsections summarize the idealized formulations used to quantify the energy input associated with each actuation type.

4.1 Power Estimation for StTW

In a mechanical implementation of StTW, an actuator performs work against the viscous stresses generated by the imposed spanwise wall motion. The power required by the control would be dominated by the mechanical inertia of the actuating system, as has been the case for most laboratory implementations so far (Auteri et al. 2010; Gatti et al. 2015). Since the estimation of power consumption strongly depends on the details of the implementation, it is common practice to assume an ideal (lossless and massless) device, so the power is transmitted to the fluid without mechanical losses. The power consumption can thus be derived from the compressible energy equation as the work performed by the spanwise wall shear per unit time:

$$P_{StTW} = \int_{A_{wall}} w_\xi \, \mu \left. \frac{\partial w}{\partial \eta} \right|_\xi \, \mathrm{d}A, \tag{15}$$

where w_w is the spanwise wall velocity and the area A_{wall}, which corresponds to the surface area where the control is applied.

4.2 Power Estimation for US

The power required for suction is governed primarily by the work needed to draw the fluid from the boundary layer and compress it to discharge conditions. To derive the expression, the flow is treated as an ideal gas undergoing isentropic compression within an idealized pump. Under these assumptions, viscous stresses may be neglected. Using the compressible energy equation and assuming that the mass flow rate through the control area and the mass flow rate at outflow conditions are equal

$$\dot{m}_{us} = \rho_{us} \, u_{us} \, l_{us} = \rho_{out} \, u_{out} \, l_{out} = \dot{m}_{out} = \dot{m}, \tag{16}$$

where the subscript us denotes the values at the wall across the boundary layer control region and out the discharge conditions. The ideal power required for suction becomes

$$P_{pump} = \int_{A_{wall}} \left\{ \dot{m} \, R T_{us} \, \frac{\gamma}{\gamma - 1} \left[\left(\frac{p_{out}}{p_{us}} \right)^{\frac{\gamma-1}{\gamma}} - 1 \right] + \frac{1}{2} \, \dot{m} u_{us}^2 \left[\left(\frac{u_{out}}{u_{us}} \right)^2 - 1 \right] \right\} \, \mathrm{d}A, \tag{17}$$

where T is the temperature, R the ideal gas constant and γ the ratio of specific heats. For this formulation, the pressure environment in which the pump operates needs to be considered. The extracted fluid is collected in a supply chamber at the pressure level $p_{chamber}$. To ensure continuous inflow through the suction area, the pressure in the chamber must be lower than the minimum pressure along the suction surface

$$p_{chamber} = min(p_{us}) - \Delta p, \tag{18}$$

where Δp accounts for the flow resistance through the porous skin and the ducts.

The fluid is expelled as a jet, assuming to recover the same total pressure as the free stream and exit with a velocity of U_∞. The associated thrust generated by the jet is

$$P_{thrust} = \dot{m}\, u_{out}. \tag{19}$$

Subtracting this contribution from the ideal pump power yields the net power input required for the suction-based control

$$P_{US} = P_{pump} - P_{thrust}. \tag{20}$$

4.3 Net Power Consumption

A direct comparison of the power requirements associated with spanwise travelling waves and wall-normal suction is not straightforward, as the underlying formulations rely on different physical assumptions and levels of idealization. For the StTW case, the power estimate reflects an ideal actuator that transfers energy without losses and performs work only against the viscous stresses generated by the imposed wall motion. This represents a highly optimistic scenario.

In contrast, the suction power model incorporates a more realistic representation of the pumping process. The fluid extracted from the boundary layer is assumed to enter a supply chamber maintained at a constant pressure level. This assumption inherently reflects non-ideal operation conditions, particularly in configurations where the surface pressure exhibits substantial spatial variations, as in transonic flow where a shock is present. In such scenarios, the pump must overcome large pressure differences, potentially increasing the power demand. However, for the present comparison, the pump efficiency is set to $\eta_{pump} = 1$ and the additional pressure drop accounting for losses due to the porous surface and the ducts is neglected ($\Delta p = 0$). These assumptions yield the most optimistic estimate permitted by the suction power formulation and ensure a more equitable comparison with the idealized StTW power evaluation.

The calculated control power is shown in Table 3. Although the absolute values depend on the specific assumptions underlying the power calculation, the results indicate that both

Table 3 Calculation of the power consumption for the two control strategies

Case ID	$\mathbf{P_{StTW}} \cdot 10^3$	$\mathbf{P_{pump}} \cdot 10^3$	$\mathbf{P_{thrust}} \cdot 10^3$	$\mathbf{P_{US}} \cdot 10^3$
SW1	1.498	-	-	-
SW2	1.939	-	-	-
SW3	0.539	-	-	-
US1	-	1.734	0.973	0.761
US2	-	1.989	1.105	0.885

control strategies require power inputs of the same order of magnitude. Nevertheless, the power associated with case US2 is approximately half that of case SW2, even though the estimate for StTW is based on more idealized assumptions.

It should be noted that these power estimates are optimistic and are intended primarily for a qualitative comparison rather than a definitive assessment of energetic efficiency. No systematic optimization of the control parameters has been performed. In the travelling wave cases, a considerable portion of the input power is irreversibly dissipated in the near-wall region, and only a small fraction of the work directly contributes to modifying the shear stress. Additionally, the relatively large amplitudes used in the travelling wave case ($A_{TW2} = 0.826$ and $A_{TW3} = 0.438$) imply rapid wall motion, which further increases the energetic costs. In contrast, the suction-based control operates on comparatively small extraction velocities ($u_{us} \approx 0.001$), resulting in a lower power consumption.

Overall, both control strategies achieve comparable improvements in aerodynamic efficiency and promote a downstream displacement of the shock. However, the power consumption associated with suction remains substantially lower than that of the spanwise travelling waves, even under the non-ideal assumptions.

5 Concluding Discussion

In this study, the aerodynamic performance and the flow characteristics of the transonic airfoil V2C with active flow control via streamwise travelling waves and boundary layer suction are investigated. To this aim, direct numerical simulations are performed to analyze the impact of both control strategies on the aerodynamic coefficients, surface distributions of the local friction and pressure, and boundary layer development, and to compare the results.

An increase in the aerodynamic efficiency is produced by both control configurations relative to the uncontrolled reference case, with maximum gains of about 12%. The lift coefficient increased in all controlled cases, while the total drag only showed small variations. The decomposition of the drag showed opposite effects for the two investigated control techniques. StTW reduce the friction drag but slightly increase the pressure drag, whereas suction produces the opposite behavior. Despite these contrasting local drag contributions, the overall aerodynamic efficiency increased in all investigated controlled cases. This suggests that the reduction of the friction drag is not the decisive factor governing the improvement of the efficiency.

It should be noted that an increase in lift, such as the one caused by the control strategies employed here, would, in a full aircraft configuration, generally be accompanied by an increase in induced drag. However, in cruise condition the dimensional value of the lift force needs to be constant and equal to the weight. Thus, the improved lift coefficient can be employed to reduce the angle of attack to restore the lift coefficient of the uncontrolled case but at a lower total drag level, including the induced drag contribution (Quadrio et al. 2022; Berizzi et al. 2025). Otherwise, the same lift force could be also obtained by exploiting the improved lift coefficient by reducing the wing chord length. This approach would make the wind more slender, with a positive effect on the induced drag, and reduce the overall weight. On the other hand, a more slender wing may be more subject to aeroelastic flutter.

A common effect of both investigated control techniques is a downstream displacement of the shock. The shift of the shock is consistently correlated with the increase in the lift

coefficient and the overall efficiency, independent of the local drag contributions. The suction velocity was tuned to match the lift coefficient of the corresponding StTW configurations, which also resulted in a similar shift of the shock position and a similar increase in the efficiency, further confirming the dominant role of the shock displacement. These findings support the hypothesis that the main mechanism responsible for the increase in aerodynamic efficiency is the delayed shock, rather than the direct reduction of the wall-shear stress. The wall-shear stress reduction is the only way in which StTW can achieve the shift of the shock position. This indicates that there may be an optimal range of control intensity. If the shock is displaced too far downstream, it could become stronger, lead to separation and an increase in pressure drag, which might result in an overall reduction of aerodynamic efficiency. Therefore, a systematic optimization of the control parameters is needed to identify the most effective configuration.

The analysis of the boundary layer parameters revealed that both investigated control mechanisms altered the displacement and the momentum thickness upstream of the shock. The control via StTW locally reduces the wall-shear stress and thus weakens the near-wall turbulence, while in the control via suction, low-momentum fluid was removed from the boundary layer, which led to a thinner boundary layer. The development and reduction of the momentum thickness before the shock seems to be the decisive factor in determining the shock position and its delay. The investigated cases with different control methods but similar c_L and shock position also show a similar momentum thickness. The two strategies of StTW and suction achieve the reduction in momentum thickness in different ways: StTW through turbulent skin-friction drag reduction, while suction via momentum flux at the wall. This observation further indicates that it is primarily the reduction in momentum thickness that leads to the shock boundary layer interaction, rather than the specific control method itself. Also, an optimization considering all aspects, such as changes in geometry, as well as the active flow control methods, is needed to get the best working configuration. Downstream of the shock region, an increase in the shape factor indicating a locally more unstable boundary layer was observed for the StTW cases, which is consistent with the observed separation and reattachment.

A comparison of the DNS results with the Euler solution, representing the inviscid limit with no boundary layer, shows the maximum possible shock displacement downstream. The thickness of the boundary layer decreases with an increasing Reynolds number, but it is still far from a vanishing boundary layer thickness. It is expected that the investigated active control methods still yield positive effects at large Reynolds numbers.

The analysis of the actuation power indicates that both control strategies operate within the same order of magnitude, although the power required for StTW is roughly twice that of the suction-based control, even under idealized assumptions. A considerable fraction of the energy in the travelling-wave case is dissipated in the near-wall region rather than contributing directly to shear-stress reduction, whereas suction relies on comparatively small suction velocities. Importantly, these power estimates are optimistic, and no systematic optimization of the control parameters has been performed. Despite these differences in energetic demand, both methods achieve comparable aerodynamic benefits.

Overall, the present study demonstrates that the control mechanisms of StTW and suction can lead to similar global aerodynamic outcomes due to their shared influence on the boundary layer thinning and shock displacement. The study thereby refines the understanding of flow control in transonic regimes, emphasizing that an increase in the aerodynamic efficiency relies primarily on manipulating the shock-boundary-layer interaction rather than

minimizing the wall-shear stress. More specifically, the results highlight that a reduction of momentum thickness and the corresponding changes in the shock boundary layer interaction are the key parameters for an increased efficiency.

A limitation of the present study is the relatively low Reynolds number of the simulations, which does not represent typical flight conditions. At such low Reynolds numbers, the boundary layer thickness is comparably large relative to the chord length, amplifying the influence of the applied control on the boundary layer development and shock position. At higher Reynolds numbers, the boundary layer becomes thinner, and the relative changes induced by the control, such as the reduction of the momentum thickness or the downstream displacement of the shock, are expected to be considerably smaller. Consequently, the overall improvement in the aerodynamic efficiency observed in the present study likely represents an upper bound, and the magnitude of the effect is expected to decrease as the Reynolds number increases. Future work could therefore focus on identifying optimal control amplitudes and the effect at higher Reynolds numbers under more realistic conditions. Such an optimization could consider both the geometric design of the airfoil and the application of active flow control, potentially leading to the most favorable aerodynamic outcome.

Appendix

A RANS Analysis of the V2C Airfoil

To complete the DNS results presented in the main manuscript, additional aerodynamic characteristics of the investigated airfoil V2C are obtained from steady RANS simulations. The computations are performed using the open-source solver SU2. A fully turbulent approach is employed using the Spalart-Allmaras turbulence model without transition modeling. The freestream conditions are identical to those used in the DNS, with a Reynolds number of $Re = 3 \times 10^5$ and a Mach number of $Ma = 0.7$. Simulations are conducted for angles of attach in the range $-1° \leq \alpha \leq 4°$.

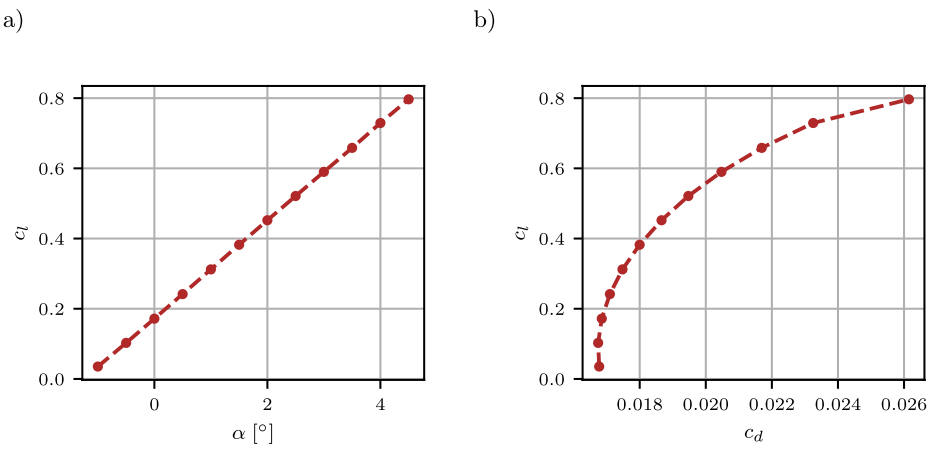

Fig. A1 Polar plots for the V2C profile with a fully turbulent approach modeled via RANS simulations

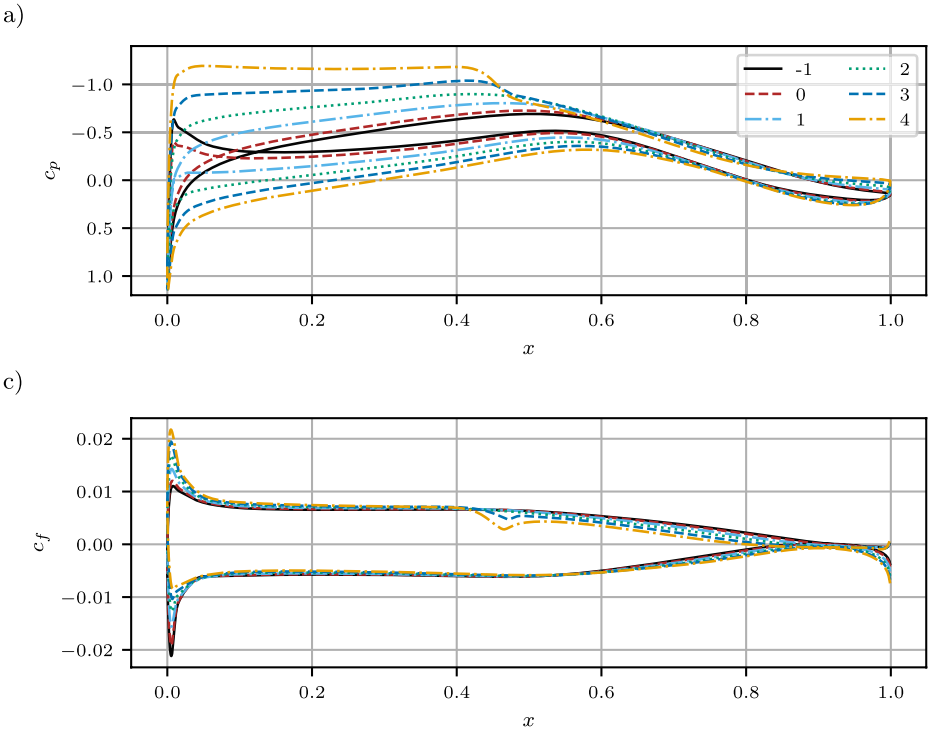

Fig. A2 (**a**) Pressure c_p and (**b**) Friction c_f coefficient distribution along the surface of the airfoil for RANS simulations with a fully turbulent approach

The resulting lift and drag polars are shown in Fig. A1. The lift coefficient exhibits a linear dependence on the angle of attack over the entire range considered. No change in the lift slope is observed, which is consistent with the assumption of a fully turbulent boundary layer in all cases. The lift coefficient obtained from the RANS simulation agrees well with the DNS results. Small differences are observed in the drag coefficient. These discrepancies are attributed to the low Reynolds number, where transition effects have a large influence on the drag. Since transition is not modeled in the present RANS setup, the drag is slightly underestimated compared to the DNS results.

The surface pressure and skin-friction distributions are presented in Fig. A2. At low angles of attack, no shock is observed. For higher angles of attack ($\alpha = 3°$ and $4°$), a shock appears on the upper surface. With increasing angle of attack, the shock strength increases, and its position shifts toward the leading edge.

The pressure distributions show a decrease in the pressure coefficient on the upper surface and an increase on the lower surface with increasing angle of attack, resulting in a larger pressure difference across the airfoil and, consequently, higher lift. The skin-friction distributions show only minor variations along most of the chord. Differences occur in the vicinity of the shock, where a local reduction in skin-friction is observed. Downstream of the shock, a decrease in the friction coefficient is present for higher angles of attack.

Acknowledgements The authors gratefully acknowledge the computing time made available to them on the high-performance computer HoreKa at the NHR Center Karlsruhe. This center is jointly supported by

the Federal Ministry of Education and Research and the state governments, for HoreKa supercomputer the Ministry of Science, Research and the Arts Baden-Württemberg.

Author Contributions AF: design of the study, DNS data, formal analysis, evaluation and discussion, writing - original draft, review and editing. GS: software, writing - review and editing. SP: supervision, writing - review and editing. NB: design of the study, writing - review and editing. MQ: supervision, writing - review and editing. DG: funding acquisition, conception, supervision, writing - review and editing.

Funding Open Access funding enabled and organized by Projekt DEAL. Financial support by the Elisabeth and Friedrich Boysen Foundation is greatly acknowledged.

Data Availability Data available on request from the authors.

Declarations

Competing Interests The authors declare no competing interests.

References

Atzori, M., Vinuesa, R., Fahland, G., Stroh, A., Gatti, D., Frohnapfel, B., Schlatter, P.: Aerodynamic effects of uniform blowing and suction on a NACA4412 airfoil. Flow Turbul. Combust. **105**(3), 735–759 (2020, Sep). https://doi.org/10.1007/s10494-020-00135-z

Auteri, F., Baron, A., Belan, M., Campanardi, G., Quadrio, M.: Experimental assessment of drag reduction by traveling waves in a turbulent pipe flow. Phys. Fluids. **22**(11) (2010, Nov). https://doi.org/10.1063/1.3491203

Banchetti, J., Luchini, P., Quadrio, M.: Turbulent drag reduction over curved walls. J Fluid Mech. **896** (2020 Aug), 896:A10. https://doi.org/10.1017/jfm.2020.338

Bechert, D.W., Bruse, M., Hage, W., Van Der Hoeven, J.G.T., Hoppe, G.: Experiments on drag-reducing surfaces and their optimization with an adjustable geometry. J Fluid Mech. **338**, 59–87 (1997). https://www.cambridge.org/core/product/identifier/S0022112096004673/type/journalarticle

Berizzi, N., Gatti, D., Soldati, G., Pirozzoli, S., Quadrio, M.: Aerodynamic performance of a transonic airfoil with spanwise forcing. J Fluid Mech. **1010**, A18 (2025, May). https://doi.org/10.1017/jfm.2025.332

Bernardini, M., Modesti, D., Salvadore, F., Pirozzoli, S.: STREAmS: a high-fidelity accelerated solver for direct numerical simulation of compressible turbulent flows. Comput. Phys. Commun. **263**, 107906 (2021, Jun). https://doi.org/10.1016/j.cpc.2021.107906

Black, T., Sarnecki, A., Mair, W.: The turbulent boundary layer with suction or injection. **20**(20) (1958)

Doerffer, P., Flaszynski, P., Dussauge, J.P., Babinsky, H., Grothe, P., Petersen, A., et al., (eds.) Transition Location Effect on Shock Wave Boundary Layer Interaction: experimental and Numerical Findings from the TFAST Project, Vol. 144 of Notes on Numerical Fluid Mechanics and Multidisciplinary Design. Springer International Publishing, Cham (2021)

Fahland, G., Stroh, A., Frohnapfel, B., Atzori, M., Vinuesa, R., Schlatter, P., Gatti, D.: Investigation of blowing and suction for turbulent flow control on airfoils. Aiaa J. **59**(11), 4422–4436 (2021, Nov). https://doi.org/10.2514/1.J060211

Frede, A., Gatti, D.: Investigation of blowing and suction for turbulent flow control on a transonic airfoil. Int J Heat Fluid Flow **113**, 109769. Elsevier BV. (2025, Jun). https://doi.org/10.1016/j.ijheatfluidflow.2025.109769

Gattere, F., Zanolini, M., Gatti, D., Bernardini, M., Quadrio, M.: Turbulent drag reduction with streamwise-travelling waves in the compressible regime. J Fluid Mech. **987**, A30 (2024). https://doi.org/10.1017/jfm.2024.408

Gatti, D., Güttler, A., Frohnapfel, B., Tropea, C.: Experimental assessment of spanwise-oscillating dielectric electroactive surfaces for turbulent drag reduction in an air channel flow. Exp Fluids **56**(5), 110 (2015, May). https://doi.org/10.1007/s00348-015-1983-x

Griffin, K.P., Fu, L., Moin, P.: General method for determining the boundary layer thickness in nonequilibrium flows. Phys. Rev. Fluids. **6**(2), 024608 (2021, Feb). https://doi.org/10.1103/PhysRevFluids.6.024608

Hwang, D.: Review of research into the concept of the microblowing technique for turbulent skin friction reduction. Prog. Aerosp. Sci. **40**(8), 559–575 (2004, Nov). https://doi.org/10.1016/j.paerosci.2005.01.002

Jung, W.J., Mangiavacchi, N., Akhavan, R.: Suppression of turbulence in wall-bounded flows by high-frequency spanwise oscillations. Phys. Fluids A: Fluid Dyn. **4**(8), 1605–1607 (1992, Aug). https://doi.org/10.1063/1.858381

Klöwer, M., Allen, M.R., Lee, D.S., Proud, S.R., Gallagher, L., Skowron, A.: Quantifying aviation's contribution to global warming. Environ. Res. Lett. **16**(10), 104027 (2021, Oct). https://doi.org/10.1088/1748-9326/ac286e

Knoop, M.W., Hartog, F.H., Schrijer, F.F.J., Van Campenhout, O.W.G., Van Nesselrooij, M., Van Oudheusden, B.W.: Experimental assessment of square-wave spatial spanwise forcing of a turbulent boundary layer. Exp Fluids **65**(5), 65 (2024, May). https://doi.org/10.1007/s00348-024-03799-9

Liu, X.D., Osher, S., Chan, T.: Weighted essentially non-oscillatory schemes. J. Comput. Phys. **115**(1), 200–212 (1994, Nov). https://doi.org/10.1006/jcph.1994.1187

Gad-el Hak M.: Flow control: passive, active, and reactive flow management., 1 edn. Cambridge University Press (2000)

Marusic, I., Chandran, D., Rouhi, A., Fu, M.K., Wine, D., Holloway, B., Chung, D., Smits, A.J.: An energy-efficient pathway to turbulent drag reduction. Nat Commun. **12**(1) (2021, Oct). https://doi.org/10.1038/s41467-021-26128-8

Mickley, H.S., Ross, R.C., Squyers, A.L., Heat, S.WE.: Mass, and momentum transfer for flow over a flat plate with blowing or suction. Naca, Tn **3208**;1–25 (1954)

Park, J., Choi, H.: Effects of uniform blowing or suction from a spanwise slot on a turbulent boundary layer flow. Phys. Fluids. **11**(10), 3095–3105 (1999, Oct). https://doi.org/10.1063/1.870167

Pirozzoli, S.: Numerical methods for high-speed flows. Annu. Rev. Fluid. Mech. **43**(1), 163–194 (2011a, Jan). https://doi.org/10.1146/annurev-fluid-122109-160718

Pirozzoli, S.: Stabilized non-dissipative approximations of Euler equations in generalized curvilinear coordinates. J. Comput. Phys. **230**(8), 2997–3014 (2011b, Apr). https://doi.org/10.1016/j.jcp.2011.01.001

Poinsot, T.J., Lelef, S.K.: Boundary conditions for direct simulations of compressible viscous flows. J. Comput. Phys. **101**(1), 104–129 (1992, Jul). https://doi.org/10.1016/0021-9991(92)90046-2

Prandtl, L., Betz, A. (eds.) Ergebnisse der Aerodynamischen Versuchsanstalt zu Göttingen - IV. Lieferung, vol. 7 of Göttinger Klassiker der Strömungmechanik. Göttingen University Press, Göttingen (1932)

Quadrio, M., Chiarini, A., Banchetti, J., Gatti, D., Memmolo, A., Pirozzoli, S.: Drag reduction on a transonic airfoil. J Fluid Mech. **942**, 2 (2022, Jul). https://doi.org/10.1017/jfm.2022.369

Quadrio, M., Ricco, P.: Critical assessment of turbulent drag reduction through spanwise wall oscillations. J Fluid Mech. **521**, 251–271 (2004, Dec). https://doi.org/10.1017/S0022112004001855

Quadrio, M., Ricco, P., Viotti, C.: Streamwise-travelling waves of spanwise wall velocity for turbulent drag reduction. J Fluid Mech. **627**, 161–178 (2009, May). https://doi.org/10.1017/S0022112009006077

Ricco, P., Skote, M., Leschziner, M.A.: A review of turbulent skin-friction drag reduction by near-wall transverse forcing. Prog. Aerosp. Sci. **123**, 100713 (2021, May). https://doi.org/10.1016/j.paerosci.2021.100713

Russo, S., Luchini, P.: A fast algorithm for the estimation of statistical error in DNS (or experimental) time averages. J. Comput. Phys. **347**(328), 328–340 (2017, Oct). 10.1016/j.jcp.2017.07.005

Schlatter, P., Örlü, R.: Assessment of direct numerical simulation data of turbulent boundary layers. J Fluid Mech. **659**(116), 116–126 (2010, Sep). https://www.cambridge.org/core/product/identifier/S0022112010003113/ type/journal article

Schlatter, P., Örlü, R.: Turbulent boundary layers at moderate Reynolds numbers: inflow length and tripping effects. J Fluid Mech. **710**, 5–34 (2012, Nov). https://doi.org/10.1017/jfm.2012.324

Soldati, G., Ceci, A., Pirozzoli, S.: FLEW: a DNS solver for compressible flows in generalized curvilinear coordinates. Aerotec. Missili Spaz. **103**(4), 413–425 (2024, Dec). https://doi.org/10.1007/s42496-024-00199-4

Spalart, P.R., McLean, J.D.: Drag reduction: enticing turbulence, and then an industry. Phil. Trans. R. Soc. A **369**(1940), 1556–1569 (2011, Apr). https://doi.org/10.1098/rsta.2010.0369.

Stroh, A., Hasegawa, Y., Schlatter, P., Frohnapfel, B.: Global effect of local skin friction drag reduction in spatially developing turbulent boundary layer. J Fluid Mech. **805**, 303–321 (2016, Oct). https://doi.org/10.1017/jfm.2016.545

Sumitani, Y., Kasagi, N.: Direct numerical simulation of turbulent transport with uniform wall injection and suction. Aiaa J. **33**(7), 1220–1228 (1995, Jul). https://doi.org/10.2514/3.12363

Szodruch, J.: Viscous drag reduction on transport aircraft. In: 29th Aerospace Sciences Meeting. American Institute of Aeronautics and Astronautics, Reno, NV, U.S.A (1991)

Visbal, M.R., Gaitonde, D.V.: On the use of higher-order finite-difference schemes on curvilinear and deforming meshes. J. Comput. Phys. **181**(1), 155–185 (2002, Sep). https://doi.org/10.1006/jcph.2002.7117

Walsh, M.J., Sellers, W.L., McGinley, C.B.: Riblet drag at flight conditions. J. Aircr. **26**(6), 570–575 (1989, Jun). https://doi.org/10.2514/3.45804

Xu, D., Ricco, P., Duan, L.: Decomposition of the skin-friction coefficient of compressible boundary layers. Phys. Fluids. **35**(3), 035107 (2023, Mar). https://doi.org/10.1063/5.0142129

Yudhistira, I., Skote, M.: Direct numerical simulation of a turbulent boundary layer over an oscillating wall. J. Turbul. **12**, (2011 Jan); 12:N9. https://doi.org/10.1080/14685248.2010.538397